Linear stability and adjoint sensitivity analysis of thermoacoustic networks with premixed flames

Alessandro Orchini*, Matthew P. Juniper

Department of Engineering, University of Cambridge, Trumpington Street, Cambridge, CB2 1PZ, UK

Abstract

We analyse the linear response of laminar conical premixed flames modelled with the linearised front-track kinematic G-equation. We start by considering the case in which the flame speed is fixed, and travelling wave velocity perturbations are advected at a speed different from the mean flow velocity. A previous study of this case contains a small error in the Flame Transfer Function (FTF), which we correct. We then allow the flame speed to depend on curvature. No analytical solutions for the FTF exist for this case so the FTF has to be calculated numerically as its parameters – aspect ratio, convection speed and Markstein length – are varied. Then we consider the stability and sensitivity of thermoacoustic systems containing these flames. Traditionally, the stability of a thermoacoustic system is found by embedding the FTF within an acoustic network model. This can be expensive, however, because the FTF must be re-calculated whenever a flame parameter is varied. Instead, we couple the linearised G-equation directly with an acoustic network model, creating a linear eigenvalue problem without explicit knowledge of the FTF. This provides a simple and quick way to analyse the stability of thermoacoustic networks. It also allows us to use adjoint sensitivity analysis to examine, at little extra cost, how the system's stability is affected by every parameter of the system.

Keywords: Premixed flame response, Flame Transfer Function, Thermoacoustic instabilities, Adjoint sensitivity analysis

1. Introduction

Thermoacoustic oscillations are one of the most persistent problems facing rocket and aircraft engine manufacturers. They occur when heat release fluctuations lock into acoustic pressure oscillations inside a combustion chamber [1, 2]. The manufacturer's ultimate aim is to design an engine that is linearly stable to thermoacoustic oscillations over the entire operating range. This is currently achieved by extensive experimental testing, repeated re-design, and sometimes by the retro-fitting of damping devices such as Helmholtz resonators. There is therefore considerable industrial motivation to develop

---

*Corresponding author

Email address: ao352@cam.ac.uk (Alessandro Orchini)

analytical and numerical tools that can predict whether thermoacoustic oscillations will occur in a system and, if so, how to change the system in order to damp them. This requires a reliable linear model of the thermoacoustic system and is aided by the application of adjoint sensitivity analysis, as described in this paper.

The stability of a thermoacoustic system is usually analysed by first calculating the Flame Transfer Function (FTF). This is the flame's heat release response to velocity, pressure, or equivalence ratio perturbations. The FTF is then combined with an acoustic network model. In this study we will focus on the response of laminar, conical flames, modelled with the linearised G-equation. Previous studies have shown that a kinematic description of the flame front, using a front-tracking version of the G-equation with a suitable velocity model, can capture the main features of the heat release response of conical premixed flames to inlet velocity fluctuations. Birbaud et al. [3] have shown that acoustic perturbations are responsible for the formation of velocity perturbations that are advected along the flame at a characteristic speed, which in general is a function of the amplitude and frequency of the forcing oscillation. A travelling wave model of axial velocity perturbations captures this phenomenon, and radial velocity fluctuations are found by choosing a divergence free flow field. In some studies in the literature the radial component was neglected, because it was shown to be less important than the axial travelling wave on the flame response [4]. The G-equation moving into a travelling wave velocity field has been shown to capture some features of conical flames dynamics - such as the formation of wrinkles on the flame surface - and the consequent heat release response.

This model has been developed and compared with experiments in several studies: [5] considered an axial dependence of the mean flow field; [6] compared the responses of conical and V-shaped flames; [7] compared FTFs from experiment with analytical results from [4, 6]; [8, 9] investigated the effect of confinement on conical flames FTFs and compared with G-equation based analytical models; [10] extracted a frequency-dependent convection speed from DNS and used it into a G-equation low-order model. For a complete review of premixed combustion and acoustic waves coupling see [11]. In this study we will assume that perturbations travel with a constant speed, which in general is different from the mean flow velocity. We also allow the flame speed to vary linearly with the local flame curvature, which avoids the formation of unphysical cusps on the flame surface. This has already been considered for V-shaped flames modelled with the G-equation [12, 13], but not for conical flames, which is a typical experimental configuration [14, 15]. The flame model we derive only captures some of the characteristics of conical flames dynamics. We do not model other effects which may be important such as gas expansion [16] and flame base motion [17] to keep the low-order flame model simple.

The analysis of FTFs helps to explain the linear dynamics of flames, such as a conical flame's low-pass characteristics. Analytical results are usually not available, however, meaning that simulations or experiments over a large range of frequencies are required, which can be expensive. This becomes even more demanding when one wants to investigate the effect of several parameters on the stability of a thermoacoustic system, because a new FTF has to be evaluated for every set of parameters. On the other hand, if a relation between the flame's heat release response and acoustic velocity or pressure fluctuations is known, one can apply classic linear stability techniques to the fully-coupled system, avoiding the explicit evaluation of flame and acoustic transfer functions [18].

The aim of this paper is to apply linear stability and adjoint sensitivity techniques to

2

a thermoacoustic network in which the flame and heat release dynamics are modelled by the kinematic G-equation. With this approach, the problem of identifying thermoacoustic instabilities is reduced to a classic eigenvalue problem of the coupled system. The resulting eigenvalue problem is small and all the eigenvalues can be calculated as the parameters of the model change. If the model were larger, a similar approach could be used, but only the eigenvalues with the largest growth rates would be calculated, using iterative methods.

Having obtained a description of the linear coupled thermoacoustic system, adjoint sensitivity analysis can be applied [19–22]. In this study we apply it to systems with premixed flames, modelled with the front-track G-equation[1] Sensitivity results can be used, for example, to calculate how to change the system in order to reduce the growth rate of each unstable eigenvalue. This change could be in the shape of the combustion chamber, the shape of the flame, or the acoustic boundary conditions. In this paper, we demonstrate the usefulness of adjoint methods by calculating how the convection speed affects the most unstable eigenvalues.

The paper is structured as follows: in §2 the linear flame model is derived. In §3 we solve the equations for the case where the flame speed is uniform and we present analytical results that correct the FTF expression contained in [4]. In §3.1 we extend the model to the more general case of curvature-dependent flame speeds. In §4 we present the fully-coupled thermoacoustic system. In §4.2 we calculate its eigenvalues while varying two parameters, build a stability map and discuss the results. Finally, in §5, we perform a sensitivity analysis on the convection speed on the entire stability map calculated with stability analysis, and provide physical insights based on these results. In §6 we summarise our study and discuss the potential applications of these methods to larger problems.

2. General framework

We describe the premixed flame's dynamics with the kinematic G-equation model, assuming that there is no density jump across the flame. This assumption precludes the Darrieus-Landau instability in the flame. This instability can cause the formation of small-scale wrinkles leading to turbulence [16, 23, 24]. This, and other physical phenomenon such as reaction mechanisms and turbulence effects, can be taken into account in an LES simulation with a G-equation formulation, see for example [25]. However, for our purposes we want to keep the model low-order, and we consider a laminar flame, assuming that the flame is an infinitely thin interface separating reactant and products and neglecting temperature variations across the flame. Under this assumption the G-equation model reads:

$$\frac{\partial \tilde{G}}{\partial \tilde{t}} + \tilde{\boldsymbol{u}} \cdot \tilde{\nabla} \tilde{G} = \tilde{s}_L^0 (1 - \mathcal{L}\tilde{\kappa}) |\tilde{\nabla}\tilde{G}|, \tag{1}$$

---

[1]Note that it would be troublesome to use this approach on the entire G-field, because the G-field itself has no physical meaning away from the G=0 level set, and care must be taken in calculating the sensitivities. This problem does not appear with a linearised formulation, because only the flame front position is tracked, which is a physical quantity.

where $\tilde{\boldsymbol{u}}$ is a prescribed flow field, $\tilde{s}_L^0$ is the propagation speed of a laminar flat flame, $\mathcal{L}$ is the Markstein length, and $\tilde{k}$ is the local flame curvature. The flame front is identified by the $\tilde{G} = 0$ level set. We describe axisymmetric flames in the laboratory framework, indicating with $\tilde{r}$ and $\tilde{x}$ the radial and axial directions respectively. We denote mean quantities with overlines and perturbations with primes. Dimensional quantities are indicated with a tilde. We also assume that the mean flow is uniform in the axial direction, and that the axial flow perturbations do not depend on the radial component. Radial velocity fluctuations are found by solving the continuity equation, assuming that the flow is incompressible. This is a well-established model that has been shown to accurately reproduce experimentally determined conical FTFs when coupled with the G-equation dynamics. Comparisons between FTFs determined from experiments and G-equation models that use this type of flow field can be found in [5, 8, 10]. Therefore we can write the two components of $\tilde{\boldsymbol{u}}$ as:

$$\tilde{u}_x = \overline{U}(1 + \epsilon u_x'(x,t)) \qquad \tilde{u}_r = -\frac{1}{2}\overline{U}\tilde{r}\epsilon\frac{\partial u_x'}{\partial \tilde{x}} \tag{2}$$

where $\epsilon \ll 1$ is the perturbation parameter, and $u_x' \sim \mathcal{O}(1)$ is the axial fluctuation, which can be forced or self-excited. We will consider forced fluctuations in order to examine how FTFs are affected by changes in flame speed due to curvature. However, we will not use these FTF results in the self-excited configuration. Instead, we will rewrite the equations in the frequency domain so that linear stability and adjoint methods can be applied without an explicit knowledge of the FTF.

Because we study small perturbations and are interested in the linear limit, it is correct to assume that the flame front is single-valued in a well-chosen reference system. The linearised conical flame front is always single valued in the laboratory framework with respect to the radial coordinate, with $\tilde{r}$ spanning the range $[0, R]$ at any instant[2]. Thus the $\tilde{G} = 0$ level set is expressed as:

$$\tilde{G}(\tilde{x},\tilde{r},\tilde{t}) = \tilde{x} - \overline{\tilde{F}}(\tilde{r}) - \epsilon\tilde{f}(\tilde{r},\tilde{t}) = 0 \tag{3}$$

where $\overline{\tilde{F}}$ and $\tilde{f}$ are the explicit functions that define the shape of the mean flame and its perturbation, respectively.

For an axisymmetric surface $\tilde{x} = S(\tilde{r})$, the mean curvature is expressed by:

$$\tilde{\kappa}(S) = \frac{\frac{d^2 S}{d\tilde{r}^2}}{\left(1 + \left(\frac{dS}{d\tilde{r}}\right)^2\right)^{3/2}} + \frac{dS}{dr}\frac{1}{r\sqrt{1 + \left(\frac{dS}{dr}\right)^2}} \tag{4}$$

---

[2]The conical flame is single valued also in the axial direction. However, to work with a function which has $\tilde{x}$ as an independent variable is an unfortunate choice, because the flame tip moves along this direction and the domain of existence of the flame front becomes time dependent, $[0, \tilde{x}_{\text{end}}(\tilde{t})]$, unnecessarily complicating the formulation [26].

Substituting eqs. (2), (3) into (1) we obtain:

$$
-\epsilon \frac{\partial \tilde{f}}{\partial \tilde{t}} + \overline{U}(1 + \epsilon u'_x) + \frac{1}{2}\overline{U}\tilde{r}\epsilon \frac{\partial u'_x}{\partial \tilde{x}}\left(\frac{d\overline{\tilde{F}}}{d\tilde{r}} + \epsilon \frac{\partial \tilde{f}}{\partial \tilde{r}}\right) =
$$
$$
= \tilde{s}_L^0 \sqrt{1 + \left(\frac{d\overline{\tilde{F}}}{d\tilde{r}} + \epsilon \frac{\partial \tilde{f}}{\partial \tilde{r}}\right)^2}\left(1 - \mathcal{L}\tilde{\kappa}\left(\overline{\tilde{F}} + \epsilon \tilde{f}\right)\right)
$$

(5)

90   where the velocity field has to be evaluated at the flame position $\tilde{x} = \overline{\tilde{F}} + \epsilon \tilde{f}$.

Geometrical inspection shows that $\sqrt{1 + (d\overline{\tilde{F}}/d\tilde{r})^2} = 1/\sin \alpha(\tilde{r})$, where $\alpha(r)$ is the internal angle that the mean flame front forms locally with the vertical axis (see Figs. 1, 3). Expanding the r.h.s. of eq. (5) in ϵ, we obtain the zero and first order equations for the flame dynamics:

$$
1 = \frac{\tilde{s}_L^0}{\overline{U}}\left[\frac{1}{\sin \alpha} - \mathcal{L}\left(\sin^2 \alpha \frac{d^2\overline{\tilde{F}}}{d\tilde{r}^2} + \frac{\frac{d\overline{\tilde{F}}}{d\tilde{r}}}{\tilde{r}}\right)\right]
$$

(6a)

$$
\frac{1}{\overline{U}}\frac{\partial \tilde{f}}{\partial \tilde{t}} - u'_x - \frac{1}{2}\tilde{r}\frac{d\overline{\tilde{F}}}{d\tilde{r}}\frac{\partial u'_x}{\partial \tilde{x}} = -\frac{\tilde{s}_L^0}{\overline{U}}\left[\sin \alpha \frac{d\overline{\tilde{F}}}{d\tilde{r}}\frac{\partial \tilde{f}}{\partial \tilde{r}} + \ldots\right.
$$
$$
\left. \ldots - \mathcal{L}\left(\sin^2 \alpha \frac{\partial^2 \tilde{f}}{\partial \tilde{r}^2} - 2\sin^4 \alpha \frac{d\overline{\tilde{F}}}{d\tilde{r}}\frac{d^2\overline{\tilde{F}}}{d\tilde{r}^2}\frac{\partial \tilde{f}}{\partial \tilde{r}} + \frac{\frac{\partial \tilde{f}}{\partial \tilde{r}}}{\tilde{r}}\right)\right]
$$

(6b)

The flame is anchored at the burner at $(\tilde{r}, \tilde{x}) = (R, 0)$ and is axisymmetric and smooth with respect to the centerline $\tilde{r} = 0$. Therefore eqs. (6) are subject to the boundary conditions:

$$
\overline{\tilde{F}}(R) = 0, \quad \left.\frac{d\overline{\tilde{F}}}{d\tilde{r}}\right|_{\tilde{r}=0} = 0, \quad \tilde{f}(R, \tilde{t}) = 0, \quad \left.\frac{\partial \tilde{f}}{\partial \tilde{r}}\right|_{\tilde{r}=0} = 0
$$

(7)

We also need to evaluate the total heat released by the flame, which is given by [2]:

$$
Q = 2\pi \rho h_r \tilde{s}_L^0 \int_0^R (1 - \mathcal{L}\tilde{k})\sqrt{1 + \left(\frac{d\overline{\tilde{F}}}{d\tilde{r}} + \epsilon \frac{\partial \tilde{f}}{\partial \tilde{r}}\right)^2}\,\tilde{r}\,d\tilde{r}
$$

(8)

Expanding the integrand in ϵ we can evaluate the steady heat release $\overline{Q}$ and the fluctuations Q'. The ratio $q' = Q'/\overline{Q}$ is the non-dimensional quantity we are interested in:

$$
q' = \frac{\int_0^R \left[\sin \alpha \frac{d\overline{\tilde{F}}}{d\tilde{r}}\frac{\partial \tilde{f}}{\partial \tilde{r}} - \mathcal{L}\left(\sin^2 \alpha \frac{\partial^2 \tilde{f}}{\partial \tilde{r}^2} - 2\sin^4 \alpha \frac{d\overline{\tilde{F}}}{d\tilde{r}}\frac{d^2\overline{\tilde{F}}}{d\tilde{r}^2}\frac{\partial \tilde{f}}{\partial \tilde{r}} + \frac{\frac{\partial \tilde{f}}{\partial \tilde{r}}}{\tilde{r}}\right)\right]\tilde{r}\,d\tilde{r}}{\int_0^R \left[\frac{1}{\sin \alpha} - \mathcal{L}\left(\sin^2 \alpha \frac{d^2\overline{\tilde{F}}}{d\tilde{r}^2} + \frac{\frac{d\overline{\tilde{F}}}{dr}}{\tilde{r}}\right)\right]\tilde{r}\,d\tilde{r}}
$$

(9)
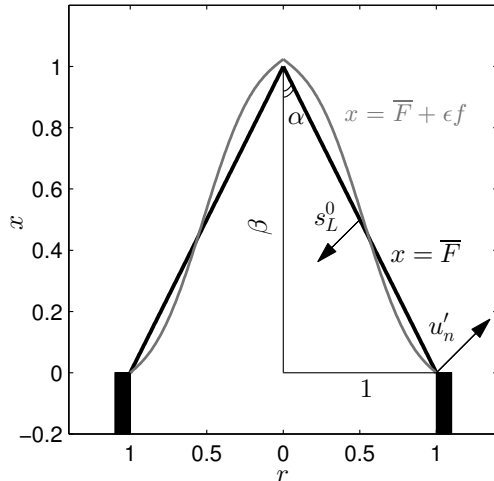
Figure 1: Schematic of the front-tracking model for a flame with constant flame speed. The steady solution is a cone on top of which the perturbation oscillates. The transfer functions are normalised by the normal velocity at the flame base.

3. Forced response to harmonic fluctuations

We first consider the following case: we impose forced, harmonic fluctuations of angular frequency ω at the flame's inlet, we assume that they are convected axially with a velocity $\overline{U}_c \neq \overline{U}$ [3], and we compute radial fluctuations assuming that the flow is incompressible [4, 10]. Therefore:

$$\tilde{u}_x = \overline{U}(1 + \epsilon \cos(\omega\tilde{t} - k\tilde{x})) \qquad \tilde{u}_r = \epsilon\frac{\overline{U}k\tilde{r}}{2}\sin(\omega\tilde{t} - k\tilde{x}) \tag{10}$$

where $k = \omega/\overline{U}_c$ is the wavenumber of the harmonic waves. For now, we neglect the contribution of the curvature on the flame speed, by setting $\mathcal{L} = 0$. This problem has already been investigated by [4]. The results we derive, however, differ slightly from the ones they obtained.

To simplify a comparison between our results and those of [4], we apply the same non-dimensional scheme to both. In particular, we scale axial lengths by the mean flame height L_f, radial lengths by the burner width R, speeds by the mean velocity $\overline{U}$, and time by the characteristic time $L_f/\overline{U}$. The complete set of non-dimensional variables, which do not have a tilde, is presented in Appendix A. The parameters relevant for this section are the ratio between the mean velocity and the convection speed K, the Strouhal number $St = \omega L_f/\overline{U}$ and the flame aspect ratio $\beta = L_f/R = [(\overline{U}^2 - \tilde{s}_L^{0^2})/\tilde{s}_L^{0^2}]^{1/2} = \cot\alpha$ (see Fig. 1).

Note that the explicit non-dimensional form of the radial velocity component is:

$$u_r = \frac{\tilde{u}_r}{\overline{U}} = \epsilon\frac{k\tilde{r}}{2}\sin(\omega\tilde{t} - k\tilde{x}) = \epsilon\frac{StKr}{2\beta}\sin[St(t - Kx)] \tag{11}$$

This is different from eq. (13) in [4], because they missed the β factor in the denominator. This missing factor affects only the results obtained by [4] using Model B. We will now

6

show how the transfer functions of heat release to harmonic velocity fluctuations changes with this correction.

When $\mathcal{L} = 0$, eq. (6a) admits an analytical solution, which in non-dimensional units is $\overline{F} = 1 - r$. The first order perturbation equation, (6b), simplifies to:

$$\frac{\partial f}{\partial t} - \frac{\beta^2}{1 + \beta^2}\frac{\partial f}{\partial r} = \cos[St(t - K(1 - r))] - \frac{1}{2}KSt\,r\sin[St(t - K(1 - r))] \qquad (12)$$

The solution of this linear PDE can be obtained, e.g., by performing a Laplace transform. The heat release fluctuations simplify to:

$$q'(t) = -\frac{2\beta^2}{1 + \beta^2}\int_0^1 \frac{\partial f}{\partial r}r\,dr = \frac{2\beta^2}{1 + \beta^2}\int_0^1 f(r,t)\,dr \qquad (13)$$

We define the Flame Transfer Function (FTF) as in [4], by:

$$G(St) = \frac{\hat{Q}'/\overline{Q}}{\hat{\tilde{u}}'_n(x = 0, r = 1)/\overline{U}\sqrt{1 + \beta^2}} \qquad (14)$$

where $\hat{\tilde{u}}'_n(x = 0, r = 1)$ is the Fourier component of the velocity normal to the flame at the flame base at angular frequency St. Introducing the parameters $\eta = K\beta^2/(1 + \beta^2)$ and $St_2 = St(1 + \beta^2)/\beta^2$, the analytical expression we obtain for the transfer function is:

$$G(St_2) = \frac{2i\left(e^{i\eta St_2} - (\eta - 1)^2 + \eta(\eta - 2)e^{iSt_2}\right) + 2St_2\eta(\eta - 1)\left(1 + \eta\left(e^{iSt_2} - 1\right)\right)}{\eta(\eta - 1)^2(2i + \eta St_2)St_2^2} \qquad (15)$$

This result can be recovered from the result of [4] Model B by setting the explicit β terms to 1 in their eq. (35), without changing the definitions of St_2 and η, which implicitly contain β. In Fig. 2 we compare our FTF with that of [4]. Differences can be observed mainly in the gain response, especially in the high-frequency region if $\eta < 1$, and in the low-frequency limit otherwise. No major differences are observed in the phase response. Also, in [8] an analytical expression for the FTF was derived using the same flow field as in eq. (10), but assuming that perturbations convect with the same speed as the mean flow, which is not necessarily the case [3, 10]. They cannot be directly compared because different scalings for the FTFs were chosen. However, we have verified that normalising the FTF with respect to axial (rather than normal to the flame) velocity fluctuations, the result we obtain in the special case $K = 1$ collapses onto the one reported by [8].

In the low-frequency limit the transfer function (15) can be expanded as:

$$G(St_2) = 1 + \frac{i}{6}(2 + 3\eta)St_2 + \mathcal{O}\left(St_2^2\right), \qquad (16)$$

and one can see that the particular case of uniformly perturbed flames, in which $\eta = 0$, yields $G(St_2) \approx 1 + \frac{i}{3}St_2$, in agreement with the results reported by [6] in the long flame limit, for which $\beta \to \infty$ and radial fluctuations are negligible according to eq. (11). We conclude this section by highlighting that, although we have presented here the correct expression for the FTF, the discussion and main results of the study conducted by [4] are unaffected.

7
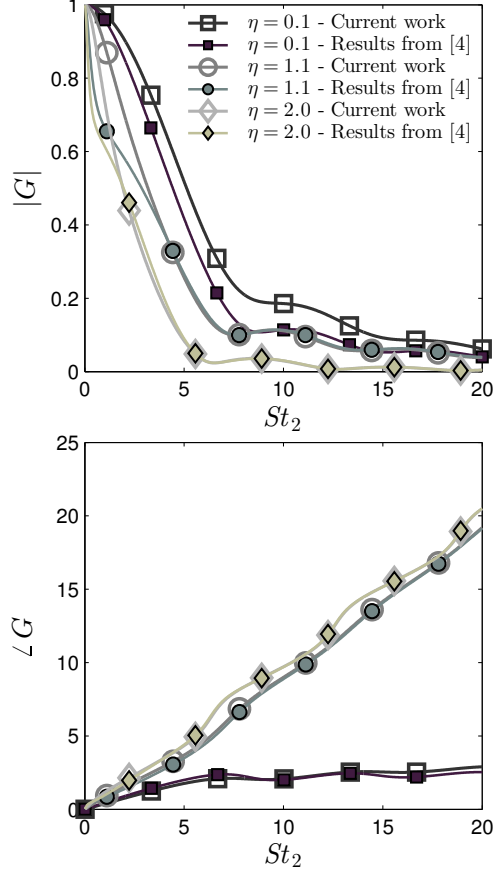
Figure 2: Gain and phase of axisymmetric, conical, Flame Transfer Functions for different values of η. Lines with empty markers correspond to our results (eq. (15)). Lines with filled markers are the results of Model B in [4]. Differences can be observed mainly in the gain response in the low- or high-frequency limit, depending on the value of η.

3.1. Curvature effects

In the previous section we derived analytical results for the special case $\mathcal{L} = 0$. We now allow the flame speed s_L to vary linearly with curvature, and use the same velocity model and non-dimensional scheme as in §3 to calculate Flame Transfer Functions. A linear curvature correction to the flame speed was originally proposed by Markstein [27] to explain the existence of stable flame fronts, which were predicted to be unconditionally unstable due to gas expansion by the constant flame speed analysis of Darrieus and Landau [23, 24]. In [16] it was shown that analogous results are obtained by accounting also for flame speed corrections due to hydrodynamic strain effects. Although we are not modelling gas expansion, a curvature dependence on the flame speed avoids the formation of unphysically sharp cusps, and it rounds the flame shape at the centerline guaranteeing continuity of the flame normals. We do not account for hydrodynamic strain effects because the flow field model we adopt is too simplistic, and only reproduces
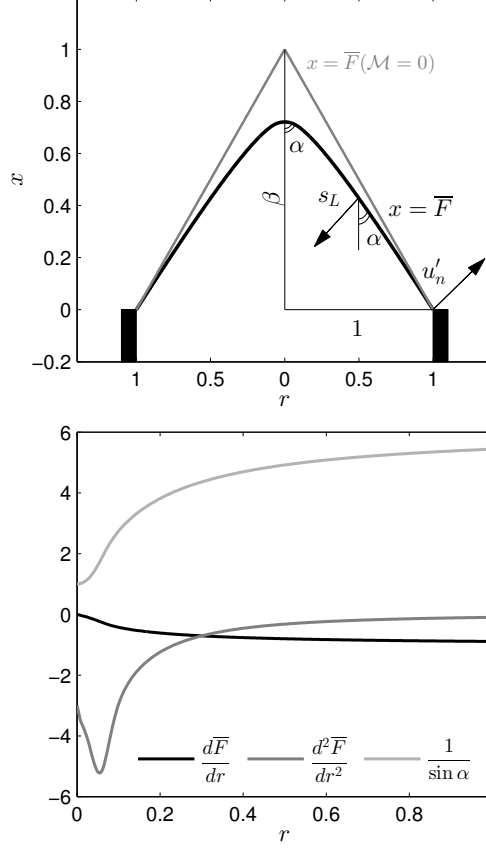
Figure 3: The steady flame shape for $\beta = 6$ and $\mathcal{M} = 0.02$. Curvature corrections to the flame speed round off the cusp at the flame tip, and the angle α now varies with respect to the radial position of the mean flame front.

138 the travelling wave form of velocity disturbances.

We introduce the non-dimensional curvature $\kappa = L_f\tilde{\kappa}$, and the Markstein number $\mathcal{M} = \mathcal{L}/L_f$. Note that the characteristic length L_f here is not the actual flame height, but is the height that the flame would have without any curvature correction to the flame speed (see Fig. 3). This is because we can find no analytical expression for the mean flame shape when $\mathcal{L} \neq 0$, and we cannot know the mean flame height *a priori*. The non-dimensional form of eqs. (6) is:

$$1 = \frac{1}{\sqrt{1+\beta^2}}\left[\frac{1}{\sin\alpha} - \mathcal{M}\beta^2\left(\sin^2\alpha\frac{d^2\overline{F}}{dr^2} + \frac{\frac{d\overline{F}}{dr}}{r}\right)\right] \tag{17a}$$

$$\frac{\partial f}{\partial t} - \cos\left[St(t - K\overline{F})\right] - StK\frac{r}{2}\frac{d\overline{F}}{dr}\sin\left[St(t - K\overline{F})\right] = -\frac{\beta^2}{\sqrt{1+\beta^2}}\times$$
$$\times\left[\sin\alpha\frac{d\overline{F}}{dr}\frac{\partial f}{\partial r} - \mathcal{M}\left(\sin^2\alpha\frac{\partial^2 f}{\partial r^2} - 2\beta^2\sin^4\alpha\frac{d\overline{F}}{dr}\frac{d^2\overline{F}}{dr^2}\frac{\partial f}{\partial r} + \frac{\frac{\partial f}{\partial r}}{r}\right)\right] \tag{17b}$$

9
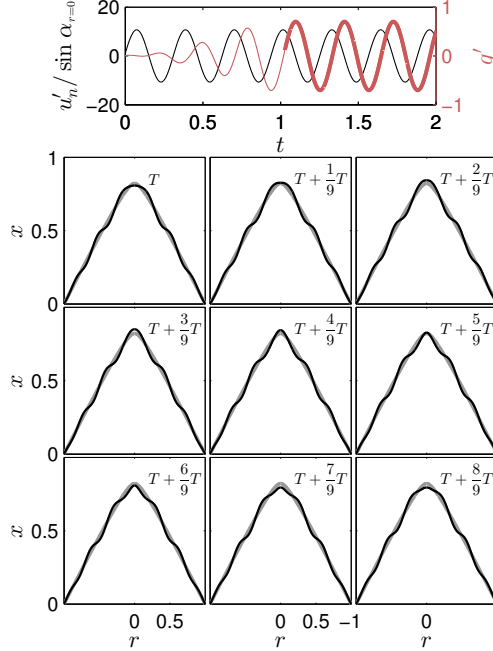
Figure 4: Time integration for $\beta = 6$, $\mathcal{M} = 0.01$, $\eta = 1.1$, and $St = 20$. Top: normal velocity at the flame base and heat release fluctuations during the transient (thin line) and steady-state solution (thick line). Bottom: evolution over a steady cycle of the perturbed flame front around the mean flame.

We require numerical integration techniques to evaluate Flame Transfer Functions when $\mathcal{L} \neq 0$. The steady eq. (17a) can be efficiently solved numerically with a Newton–Raphson method. The mean quantities $d\overline{F}/dr$, $d^2\overline{F}/dr^2$, $\sin\alpha$ (Fig. 3), and the perturbation f are discretized in space using a second-order finite difference scheme. The linear PDE (17b) is then marched forward in time using an explicit third-order Runge-Kutta method [28]. The final time is sufficiently large for the transient behaviour to disappear, and for a few forced cycles to fully travel along the mean flame (Fig. 4). The steady-state heat release fluctuations q' are evaluated according to eq. (9) at every time step. The Flame Transfer Function definition generalises eq. (14):

$$G^{\mathcal{M}}(St) = \frac{\hat{q}'}{\hat{u}'_n(x=0, r=1)\sqrt{1 + \beta^2 \left(\frac{d\overline{F}}{dr}\right)^2_{r=1}}} \tag{18}$$

where

$$\hat{u}'_n(x=0, r=1) = \left. \frac{\hat{u}'_x - \beta\frac{d\overline{F}}{dr}\hat{u}'_r}{\sqrt{1 + \beta^2 \left(\frac{d\overline{F}}{dr}\right)^2}} \right|_{x=0, r=1} \tag{19}$$

139 is the velocity component normal to the mean flame at the flame base.

140 The numerical code has been benchmarked against theoretically known perturbed
141 flame evolutions such as eq. (12), and transfer functions such as (15), showing that the

10
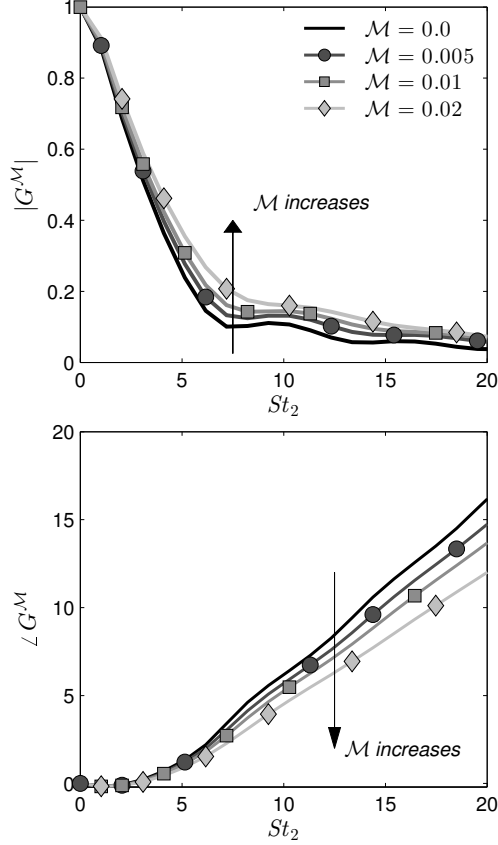
Figure 5: Transfer functions of conical flames with curvature-dependent flame speed. Gain and phase for $\beta = 6$, $\eta = 1.1$, and different $\mathcal{M}$. Increasing the Markstein number decreases the flame's mean height. As a consequence the time delay of perturbations lowers (shifts in phase), and in the low-frequency limit increases the effect of small perturbation on the heat release.

numerical results for gain and phase converge to the correct values in proportion to Δr^2, where Δr is the grid spacing used in the discretization scheme. Fig. 4 shows the integrated heat release and normal velocity time-traces during the transient and steady-state solutions of the forced system. The gain and phase can be calculated by taking the ratio between the steady-state amplitudes and the (normalised) distance between the peaks of the time series respectively. In the bottom panels the evolution of the perturbed flame front around the mean flame front is shown over a forced cycle.

The higher the frequency of the forcing fluctuations, the smaller the wavelengths of the perturbations that are generated on the flame. This has a consequence for the numerical cost required to evaluate the transfer functions: at high-frequencies, the perturbation wavelengths are shorter and the grid spacing Δr has to be smaller. The time step decreases accordingly and the time-marching integration can become expensive. This phenomenon partly justifies the technique developed in §4.

Fig. 5 shows the heat release transfer function for $\beta = 6$ and $\eta = 1.1$ while increasing

11

the Markstein length. At small frequencies the perturbed flame is not highly wrinkled and
first order curvature effects are small. At the same time, when the Markstein length is
larger, the flame slope $d\overline{F}/dr$ at the base is smaller (see Fig. 3). Therefore, the projection
of the radial velocity onto the flame's normal reduces, the denominator in eq. (18) reduces,
and the FTF gain increases. At higher frequencies the flame is highly wrinkled and
curvature corrections play a crucial role in reducing the size of these wrinkles, which
lowers the gain. These arguments are consistent with the gain's dependence on $\mathcal{M}$
shown in Fig. 5. Furthermore, the fact that the FTF phase shifts towards zero with $\mathcal{M}$
has a clear physical cause: when the Markstein number is larger, the flame is shorter and
the perturbations take less time to travel along the flame.
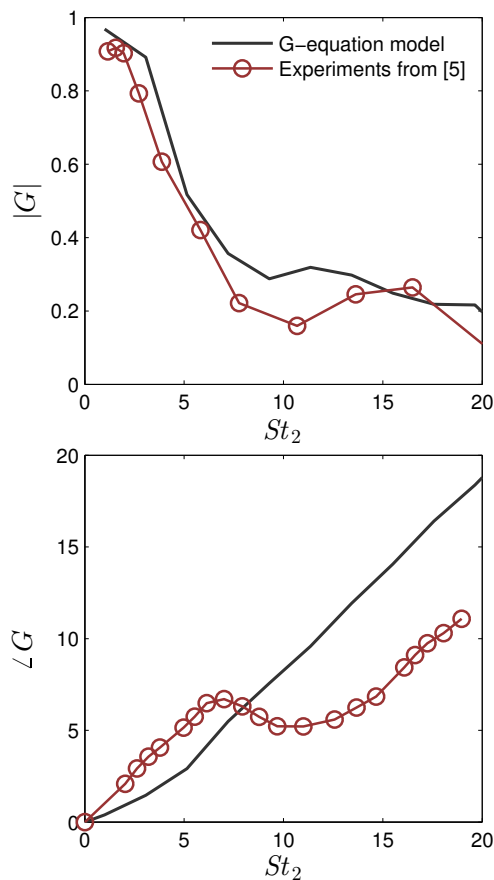
Figure 6: Comparison between our low-order model and an experimentally determined [5] FTF. The
FTFs here are scaled with respect to axial velocity fluctuations. Parameters for the simulation were
chosen to match experimental values; the gain responses compare reasonably well, especially at low
frequencies, whereas we cannot capture the phase inflection because we fix the convection speed value.

As shown in Fig. 5, curvature corrections to the FTF are small, and comparisons
between the G-equation model without curvature effects and experiments can be found
in the literature [5, 7, 8, 10]. Nonetheless, in Fig. 6 we compare the FTF derived from

our model (with curvature correction) with that determined from experiments, extracted from [5]. The flame aspect ratio was set to $\beta = 2.64$, and was derived by imposing a mean velocity $\overline{U} = 1.1$ m/s and a flame speed $s_L^0 = 0.39$ m/s, as suggested in [5]. Because we have no information on the other parameters, we set the convection speed ratio and the Markstein length to the reasonable values $K = 1.2$ and $\mathcal{M} = 0.01$ respectively [10]. Note that, in order to compare the results, in Fig. 6 we have scaled the FTF with respect to axial velocity fluctuations, and not to normal velocity at the flame base as in the rest of this study. The gains compare reasonably well, especially at low frequencies, which is a known result [6, 8]. The phase response difference may be adjusted at low frequencies by choosing a suitable value for K. However, our current model cannot capture the inflection that occurs at $St_2 \approx 7.5$, because we are fixing the value of K. To capture this phenomenon, a possibility would be to use a frequency dependent convection speed extracted from experiments or DNS as in [10]. However, we also note that the inflection of the phase response is not always observed in experiments. For example in [7, 8] the phase is shown to increase linearly and to saturate at high frequencies. In this study we do not aim to accurately reproduce a specific experiment, and in the following we will retain K constant.

As a final remark, we note that in [29] was shown that turbulence effects on the flame dynamics – modelled with a low-intense stochastic component in the velocity field – are analogous to curvatures effects on the flame speed (and consequent dynamics) of the ensemble-averaged flame front. Using their result, we can thus expect an analogy between the curvature corrections to FTFs discussed above and variations in the FTFs of flames with small turbulent fluctuations.

4. Self-excited problem

So far, we have investigated the forced response of conical premixed flames to harmonic fluctuations. Although the knowledge of Flame Transfer Functions has an importance, usually one is interested in the analysis of a closed flame-flow-acoustics feedback loop. In this context the flame dynamics is not forced, but is coupled with the acoustic equations and the flow field dynamics. Perturbations will grow unboundedly in time if and only if at least one thermoacoustic mode has a positive growth rate. If a model that couples fluid and combustion fluctuations is prescribed, then explicit knowledge of the FTF is not needed in order to assess the system's stability. Indeed, one can simply construct a larger eigenvalue problem, whose state vector contains all the variables of the fully-coupled flame-acoustic system, and use Arnoldi methods to calculate the eigenvalues with the largest growth rate. As we will show in §5, this formulation also allows for straightforwardly using adjoint methods to calculate eigenvalues sensitivities with respect to any system's parameter. The latter is precluded when a numerically (or experimentally) measured FTF is used, because the explicit dependence of the linear operator on the base state and system's parameters is unknown. In the following we will describe the method using the same G-equation model as presented in §2, but it could as well be used in a network with a higher order model for the premixed flame, as the ones developed by [30] or [31].

To keep the model low-order, we divide the thermoacoustic problem conceptually into three components, which are connected in a feedback loop: (i) the flame and heat release fluctuations dynamics are governed by the kinematic, linear G-equation (eqs. (6b)

13

214 and (9)); (ii) the heat release acts as a point source in the (linear) acoustic equations.
215 Unsteady heat dilates the surrounding air and is a monopole source of acoustic waves,
216 which in turn provoke velocity fluctuations at the flame base [32–35]; (iii) axial velocity
217 fluctuations are convected downstream in the flame domain, and radial fluctuations are
218 calculated to guarantee mass conservation [4, 10].

The acoustic equations can conveniently be written in state-space form as:

$$\frac{d\boldsymbol{s}}{dt} = \mathcal{A}\boldsymbol{s} + \mathcal{B}q'(t) \tag{20a}$$

$$u'_x = \mathcal{C}_u\boldsymbol{s}, \qquad p' = \mathcal{C}_p\boldsymbol{s} \tag{20b}$$

where $\boldsymbol{s}$ is the state vector, and $\mathcal{A}$, $\mathcal{B}$ and $\mathcal{C}$ are the system, input and output matrices respectively. Eqs. (20) are scaled in non-dimensional units consistently with (A.1). Typical non-dimensional numbers that appear in the matrices are the mean flow Mach number $\overline{M} = \overline{U}/c$, where c is the speed of sound, and the ratio between the flame and acoustic characteristic lengths. We refer to [32, 35] for a derivation of the acoustic equations in this form. In the Laplace space, the acoustic transfer function can be expressed as:

$$G_u^{ac}(s) = \frac{u'_x(s)}{q'(s)} = \mathcal{C}_u\left(s\mathcal{I} - \mathcal{A}\right)^{-1}\mathcal{B} \tag{21}$$

219 where s is the Laplace variable. Note that it is unimportant how the state-space model
220 has been derived from the acoustic equations. One can use a Galerkin decomposition in
221 Fourier modes as in [1, 33], a state vector with memory as in [36] or Padé approximations
222 as in [35, 37].

Finally, the convective model for the velocity field reads:

$$\frac{\partial u'_x}{\partial t} + \frac{1}{K}\frac{\partial u'_x}{\partial x} = 0, \qquad u'_x(x = 0, t) = \mathcal{C}_u\boldsymbol{s}(t) \tag{22}$$

223 where the second equation corresponds to the boundary condition that the axial velocity
224 at the flame base is given by the acoustic state-space model.

225 *4.1. Eigenvalue problem*

Because we are interested in finding the unstable modes of the coupled system, we look for solutions of the type $f(r,t) = \hat{f}(r)e^{\lambda t}$, $\boldsymbol{s}(t) = \hat{\boldsymbol{s}}e^{\lambda t}$, $u'_x(x,t) = \hat{u}'_x(x)e^{\lambda t}$. We then discretize $\overline{F}$, $\hat{f}$, and $\hat{u}'_x$ in space, as well as the derivative and integral operators, and combine the discrete versions of eqs. (6b), (9), (20), (22) to obtain:

$$M\boldsymbol{z} = \lambda\boldsymbol{z} \tag{23}$$

where $\lambda = \sigma + iSt$ are the complex eigenvalues sought, $\boldsymbol{z}$ defines the thermoacoustic state as $\boldsymbol{z} = \left[\hat{f}^1, \ldots, \hat{f}^{N_r}, \hat{s}^1, \ldots, \hat{s}^M, \hat{u}'^1_x, \ldots, \hat{u}'^{N_x}_x\right]^T$, and the matrix M can be written as

$$M = \left[\begin{array}{ccc} M_{ff} & M_{fs} & M_{fu} \\ M_{sf} & M_{ss} & M_{su} \\ M_{uf} & M_{us} & M_{uu} \end{array}\right], \tag{24}$$

14

226 where the submatrix M_{ff} represents the coupling between the flame evolution and the
227 flame state, M_{fs} represents the coupling between the flame evolution and the acoustic
228 state, and so on. Their explicit expressions are given in Appendix B.

We observe that eq. (22) could be analytically solved, yielding:

$$\hat{u}'_x(x) = \mathcal{C}_u \hat{s} e^{-\lambda K x} = \mathcal{C}_u \left(\lambda \mathcal{I} - A\right)^{-1} \mathcal{B} e^{-\lambda K x} \hat{q} \tag{25}$$

229 where we have used eq. (21) in the second equality. Note that the eigenvalue λ appears
230 both in the exponential and in the matrix inversion operation. Because of this, if we
231 were to substitute the velocity field expression into the flame dynamics we would obtain
232 a smaller eigenvalue problem – the state would be fully determined by the flame shape $\hat{f}$ –
233 but the problem would be nonlinear. Because of the small size of the eigenvalue problems
234 we are solving, we have decided to solve the larger but linear eigenvalue problem (23).

By solving the eigenvalue problem, we can determine whether, for a given acoustic
configuration and set of flame/flow parameters, there exist modes with a positive growth
rate. We can determine their frequencies without having explicit knowledge of the Flame
Transfer Function. This is useful because we do not need to evaluate a new FTF if we
change a flame parameter, and we can investigate a large set of parameters at a lower
computational cost. Numerical cost for the evaluation of FTFs becomes large at high-
frequencies, where the wavelengths are short and the CFL condition for the time step
gives:

$$\Delta t < \text{CFL} \frac{\Delta r}{U} \approx \text{CFL} \frac{1 + \beta^2}{\beta^2} \frac{\Delta r^2}{\Delta r + \mathcal{M} \frac{2 + \beta^2}{\sqrt{1 + \beta^2}}} \tag{26}$$

235 where the advection velocity U can be estimated from eq. (B.1a). For non-small curvature
236 effects, the time step scales as Δr^2, and evaluating transfer functions at high frequencies
237 becomes numerically expensive. Also, the dimension of the eigenvalue matrix M increases
238 at high-frequencies because the spatial discretization has to be very dense in order to
239 capture small wavelengths fluctuations. We are not interested in determining all the
240 eigenvalues of the matrix, however, but only those with the most positive real parts.
241 Thus one can use numerical algorithms such as Arnoldi methods to compute the few
242 eigenvalues of interest, greatly reducing the cost of the problem.

243 *4.2. Stability of a ducted flame*

244 We now consider the case of a flame confined in a duct. The state-space matrices for
245 the acoustics are derived from the linearised Euler equations with a wave-based approach.
246 They are the same as in [35] – to which we refer for a detailed description of the state-
247 space model derivation – so that we can benchmark our linear code against this previous
248 study, as discussed in the next paragraphs. The acoustic geometry consists of a straight
249 pipe whose radius abruptly increases at the flame location to emulate the blockage of
250 the burner upstream of the flame. The acoustic mean properties suddenly vary across
251 the flame and across area variations to satisfy mass, momentum and energy balances.
252 We impose a closed perfectly reflecting boundary condition at the inlet and an open
253 frequency dependent reflection coefficient at the outlet.

254 The network model acoustic parameters were inspired by the experimental setup of
255 Kabiraj et al. [15], but our aim here is not to accurately reproduce their results. This
256 study focuses on linear stability and sensitivity analysis, and not on nonlinear dynamics;

15

furthermore our flame model is too simplistic to predict precisely the system's Hopf bifurcations. This is discussed more in details in [35], where a fully-nonlinear analysis on this model was performed, a qualitative comparison between the numerical study and the experimental results was reported, and limits and possible improvements to the model were discussed. It was found that the flame motion over a self-excited limit cycle resembles the experimental one: Fig. 11 of [15], which refers to periodic flame motion after the first Hopf bifurcation, can be compared with the top row of Fig. 10 in [35]. Also, comparable oscillation frequencies in self-excited oscillations were found, and the same set of bifurcations ultimately leading to chaotic motion was observed.

We fix the flame parameters to $K = 1.2$ and $\mathcal{M} = 0.02$, the ratio between the downstream and upstream acoustic duct diameters to $D_2/D_1 = 1.75$, the temperature jump across the flame to $T_2/T_1 = 2$, and the Mach number in the cold region to $M = 0.0057$. Fixing K has a strong influence on the flame time lag response. Experiments and DNS have shown that the convection speed ratio K is in general a function of the perturbation amplitude and frequency [3, 10]. For simplicity we decided to fix K to a reasonable value that fits their findings. Similar values have been used in other numerical analysis [33–35]. The value chosen for T_2 has to represent the mean temperature in the downstream part of the duct. This number should be a function of the flame position in the duct: the more downstream is the flame, the higher is the mean temperature in the last section, because less heat is dissipated through the walls. Nonetheless, we decide to keep this parameter independent from the flame location for simplicity.

The first bifurcation parameter we investigate is the position of the flame in the duct $x_f \in [0, 1]$, fixing the flame aspect ratio to $\beta = 6$. This set of parameters corresponds to the one considered in [35], for which a Flame Describing Function (FDF) has been evaluated, and a nonlinear stability analysis has been performed with different methods. The corresponding FTF is analogous to the one shown in Fig. 5 for $\mathcal{M} = 0.02$. We can take advantage of the fact that (i) its gain never exceeds unity, and (ii) it acts as a low-pass filter, to deduce that if a thermoacoustic mode has a positive growth rate, then (i) it is associated with one of the acoustic resonant frequencies, for which the gain is much larger than one and (ii) it is a low-frequency mode. This was indeed shown to be true in [35] also in the nonlinear limit, by means of the harmonic balance technique. Only modes associated with the first two acoustic resonant frequencies were found to be unstable. Therefore, we can reduce the size of the eigenvalue problem by using a small state-space model that characterizes only the first few acoustic modes ($N_s = 4$), and by using a relatively large grid spacing Δr, because we do not need to describe short wavelengths ($N_r = N_x = 399$).

Fig. 7 shows the results of the eigenvalue problem. Only the growth rates $\sigma^* = \sigma/(2\pi)$ and frequencies $St^* = St/(2\pi)$ of the eigenvalues with a non-negative real part are shown. We clearly identify two modes, whose frequencies can be shown to be very close to the first and second acoustic resonant frequencies. We have verified with convergence tests that these modes are physical modes, and not spurious modes that arise because of the discretization of the equations. We observe that for some flame positions, x_f, both modes may have a positive growth rate. We have indicated with squares the Hopf bifurcations of the high-frequency mode, which lie inside the region of instability of the low-frequency mode. When both modes have a positive real part, the growth rate of the of the low-frequency mode dominates over the growth rate of the high-frequency one, which is consistent with the system's low-pass characteristics. All these results agree with the

16
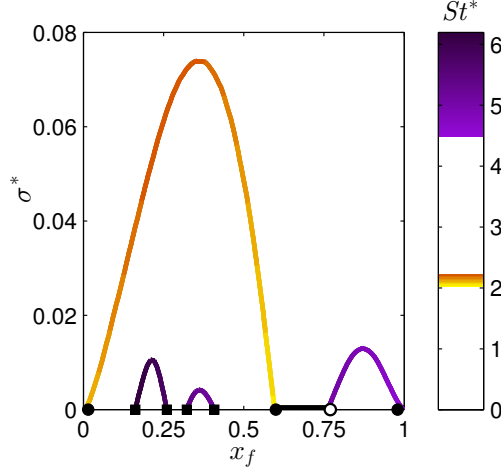
Figure 7: Growth rates of the eigenvalues λ with a non-negative real part. A line's colour indicates the frequency of the mode. Thick lines and circles at $\sigma^* = 0$ correspond to brute-force time marching results described in [35]. Full and empty circles correspond to super- and subcritical Hopf bifurcations respectively.

fully nonlinear analysis carried out by [35]. We have plotted in Fig. 7 with thick black lines and circles the linearly stable regions identified by brute-force time marching of the fully nonlinear equations. According to these results, filled and empty circles locate super- and subcritical Hopf bifurcations respectively.
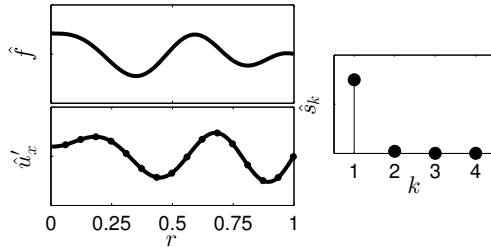
Figure 8: Real parts of the eigenstate of the unstable mode for $x_f = 0.27$. Top left: perturbed flame shape state. Bottom left: axial velocity fluctuations. Right: components of the acoustic state space vector.

Fig. 8 shows the eigenvector of the unstable mode at $x_f = 0.27$. Moving from the flame anchoring point $r = 1$ to the centreline $r = 0$, the top-left frame shows that the flame perturbation grows in amplitude spatially. On the other hand, velocity fluctuations, shown in the bottom panel, decrease in amplitude while moving in the same direction. This is physically correct because we are using a convective model with speed $1/K$, so the velocity amplitude at $r = 0$ at time t is the amplitude that the velocity perturbation had at $r = 1$ at time $t - 1/K$, because λ has a positive growth rate, the earlier perturbation had a smaller amplitude than the current one. We showed in eq. (25) the analytical solution for the convective model along the flame. The analytical result is plotted with

circles in Fig. 8, and is in perfect agreement with the numerically evaluated eigenstate. This comparison can be used as a test to assess the convergence of the eigenvalue problem. For example, high-frequency modes will not converge with the current grid-space size but we know that they will be stable because the flame acts as a low-pass filter. Finally, the right panel shows the intensity of the acoustic eigenstate. The fact that only the first mode has a large intensity is an indicator of the fact that this thermoacoustic mode is closely linked to the first acoustic resonant mode.

Given the relatively small size of the eigenvalue problem, we can quickly calculate the stability of the thermoacoustic system for a wide range of parameters. We start by focusing on two parameters: the position of the flame in the duct and the flame aspect ratio β, which can also be interpreted as the ratio between the flame speed and the mean flow velocity (see eqs. (A.1)). We vary x_f along the full length of the duct in steps of $\Delta x_f = 0.01$, and β in the range $[0.5, 10]$ in steps of $\Delta\beta = 0.1$. For each couple of parameters, we solve the eigenvalue problem (23), and we investigate the two eigenmodes with the largest growth rate. We will refer to the low- and high-frequency modes as Mode 1 and Mode 2 respectively because they are closely linked to the acoustic fundamental and first harmonic resonant modes. Note that we are not tracking the eigenvalues, but we are just looking at the two eigenvalues with the largest growth rate. We find that, in our system, some of the eigenvalues may cross in the complex plane while varying the bifurcation parameters. Because they cross, the growth rate map we evaluate is continuous, but its derivative is not, as is discussed in §5. We have verified that the eigenvalue crossing always occurs when the growth rates of the crossing modes are negative (dashed lines in Fig. 9), and we are not missing any region of instability in the following analysis.

The growth rate maps of the two modes are shown in Fig. 9. We have highlighted with black lines the zero growth rate contours, which are the neutral curves along which Hopf bifurcations are located. The thin straight lines (and circles) at $\beta = 6$ on the two maps correspond to the growth rates (and Hopf bifurcations) shown in Fig. 7. Note that we have used two different colour maps for the stability diagrams of the two modes to highlight that the growth rate of Mode 1 is higher than the growth rate of Mode 2, which agrees with the fact that the flame acts as a low-pass filter.

Looking at the size of the regions with positive (or negative) growth rates, we observe that Mode 1 shows very large zones in which the sign of the growth rate does not change, and they approximately extend over the whole length of the duct. On the other hand, Mode 2 shows several smaller regions with a positive growth rate, and they extend approximately over $1/3$ of the duct.

This can be explained by looking at the shape of the acoustic modes. Because the acoustic network has a temperature jump across the flame and a cross sectional area variation, the shape of the modes is different for every value of x_f. However, our network can be roughly approximated by a closed-open pipe with no area or temperature variations, as shown in Fig. 10. In Mode 1, the interaction between pressure and velocity acoustic waves has nodes at the boundaries and a maxima (or minima) is found at the centre of the duct. For the second mode, the acoustics waves have nodes at $x_f = 1/3$ and $2/3$, and maxima or minima are found at $x_f = 1/4, 2/4, 3/4$. These same patterns can be observed (with some modifications due to temperature and area variations of the acoustic network we are considering) in the growth rate maps of the two thermoacoustic modes.
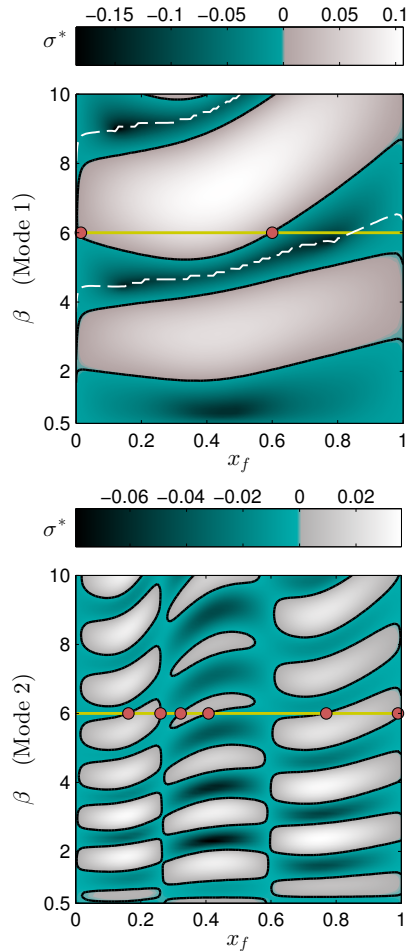
Figure 9: Growth rate maps of two thermoacoustic modes. Dark regions are associated with a negative growth rate (the mode is stable), and light regions with positive growth rates (the mode is unstable). Two different colour maps are used to highlight the growth rate differences. Neutral lines (zero growth rate) are highlighted in black. The straight thin line and the circles correspond to the results and the Hopf bifurcations shown in Fig. 7. In Mode 1 we observe an eigenvalue crossing phenomenon: the curves along which the eigenvalues cross are highlighted with dashed white lines.

5. Sensitivity to convection speed

Having evaluated steady solutions and the stability of small perturbations around them over a fairly large parameter space, a natural question that arises is: how does the stability map change by making a tiny change to one of the parameters in the governing equations? This information is contained in the so-called base state sensitivity map, which measures the drift of the eigenvalues $\delta\lambda$ with respect to a given perturbation in a parameter δK [19, 20, 38]. Adjoint methods for eigenvalue sensitivity were introduced in thermoacoustics by [21] on a Rijke tube system, and extended to the analysis of enclosed diffusion flames with a Fourier-Galerkin based acoustics by [22]. Here we calculate

19
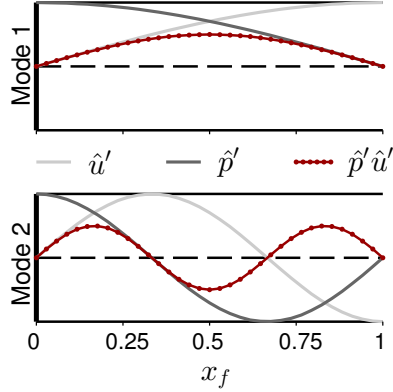
Figure 10: Fundamental and first harmonic modes in a closed-open pipe, which roughly approximates the acoustic network under consideration. In the first harmonic mode, velocity and pressure have nodes at $x_f = 1/3, 2/3$.

eigenvalue sensitivities on a wave-based acoustic network with a premixed flame model. This is indispensable information for gradient-based optimization algorithms, in which one changes the flame or cavity shape to minimize the growth rate of a particular mode.

To perform a sensitivity analysis, we need to define the adjoint operator of the direct equations (23). We can either derive the continuous adjoint equations from the continuous governing equations, or we can obtain a discrete version of the adjoint equations directly from the discretized version of the direct equations [21, 39]. Here we will use the second approach, i.e., we will define the adjoint matrix $M^\dagger$ to be $M^\dagger = M^H$, where the superscript ^{H} stands for Hermitian conjugation. Under this assumption, the drift in the eigenvalue is given by the known relation [19, 20]:

$$\delta \lambda_i = \frac{\left\langle \boldsymbol{z}_i^\dagger, \delta M \boldsymbol{z}_i \right\rangle}{\left\langle \boldsymbol{z}_i^\dagger, \boldsymbol{z}_i \right\rangle} \qquad (27)$$

where $\boldsymbol{z}_i$ is a right eigenvector of the direct matrix, $M \boldsymbol{z}_i = \lambda_i \boldsymbol{z}_i$, and $\boldsymbol{z}_i^\dagger$ is the corresponding right eigenvector of the adjoint matrix, $M^H \boldsymbol{z}_i^\dagger = \lambda_i^* \boldsymbol{z}_i^\dagger$, where the superscript * stands for complex conjugation. The symbol $\langle \cdot, \cdot \rangle$ defines an inner product. To define the adjoint discrete operator as the transpose conjugate of the direct discrete operator, is equivalent to choosing the scalar product as an inner product, i.e.:

$$\langle \boldsymbol{z}_1, \boldsymbol{z}_2 \rangle = \boldsymbol{z}_1^H \cdot \boldsymbol{z}_2 = \sum_{i=1}^{N_r + N_s + N_x} z_1^{i^*} z_2^i \qquad (28)$$

Note that here we are only interested in evaluating sensitivities of the eigenvalues. The drift in the eigenvalue is a well-defined physical quantity, and can be proven to be independent of the choice of the inner product [20]. This choice allows a very simple connection between the adjoint right eigenvectors $\boldsymbol{z}^\dagger$ and the left eigenvectors $\boldsymbol{z}_L$ of the direct matrix M. In particular we have that $\boldsymbol{z}^\dagger = \boldsymbol{z}_L^H$, meaning that, by computing both

20

the right and left eigenvectors of M, we have all the information required to evaluate sensitivities. Finally, recall that M is the discrete operator of the governing equations linearised around a steady solution. Indicating the base state with $\overline{z}$, the eigenvalue drift with respect to parameter p is:

$$\delta\lambda = \frac{z_L \cdot \delta M(\overline{z}, p)z}{z_L \cdot z} = \left(\frac{z_L \cdot \frac{\partial M}{\partial p} z}{z_L \cdot z} + \frac{z_L \cdot \frac{\partial M}{\partial \overline{z}} \frac{\partial \overline{z}}{\partial p} z}{z_L \cdot z} \right) \delta p \qquad (29)$$

376 where we have used the chain rule to account for the fact that the steady state is in general
377 a function of the parameter p as well. The quantity $\frac{\partial \overline{z}}{\partial p}$ cannot be easily evaluated in
378 general, and another adjoint problem can be set up to calculate it. The left and right
379 eigenvectors of M have already been evaluated when solving the eigenproblem (23).
380 Therefore, with simple matrix multiplication operations, we can compute the sensitivity
381 of the system with respect to *any* parameter.

382   In this paper we will focus on the role of the convection speed, K, on the stability
383 of the system. This parameter does not affect the steady solution so the sensitivity is
384 simply given by the first term in the r.h.s of eq (29). The convection speed is of crucial
385 importance in modelling premixed flames and it has been investigated by [4, 10]. In [40]
386 it is shown that it severely affects the gain response of non-conical Flame Describing
387 Functions. The matrix $\frac{\partial M}{\partial K}$ can be evaluated explicitly from eqs. (B.5), and only the
388 derivatives of the blocks (B.5h) and (B.5i) are non-zero.
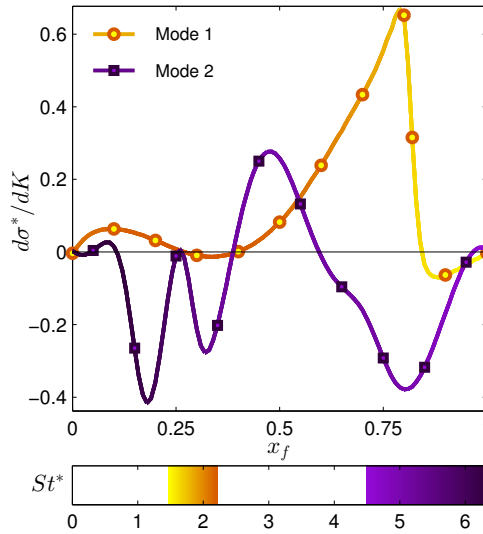
Figure 11: Growth rate sensitivity at $\beta = 6$ of the two modes with the largest growth rate to convection speed perturbations. Lines correspond to sensitivity calculations with adjoint methods; the line's colour refers to the frequency of the unperturbed modes. Markers refer to sensitivity calculations with a finite difference approach, and validate the adjoint calculations.

389   It is known that the adjoint eigenvectors of the finite-difference discretized equations
390 can be noisy close to non-Dirichlet boundary conditions [39, 41]. This is because the
391 discrete forms of the boundary conditions have been chosen to work well with the right

21

eigenvectors, but there is no guarantee that they will work with the same accuracy on the left ones. Indeed, we observe some noise in the left eigenvectors of M close to the Neumann boundary condition relative to the flame tip, so we first validate the adjoint-based sensitivity results with a brute-force finite difference method.

Using the same parameters as in §4.2, and fixing $\beta = 6$, we show in Fig. 11 the growth rate sensitivity to variations in the convection speed evaluated with adjoint-based (solid lines) and finite-difference (markers) methods for thermoacoustic modes 1 and 2. Although we observe some noise in the adjoint eigenvectors close to the flame Neumann boundary condition (not shown), the results obtained with the two methods agree perfectly. From now on we will always refer to the adjoint-based sensitivity results. At a given x_f location in Fig. 11, if the sensitivity of a mode is positive, then a small decrease of the parameter K will make the growth rate smaller and vice versa. Note that a change in K could make one mode grow and another mode decay. This is typically a disadvantageous result, because a change that tends to stabilise one mode may destabilise another one. Also, at this stage, no clear pattern can be observed for the behaviour of the two modes.

To gain more insight into the physical mechanisms that trigger the instabilities, we extend the growth rate sensitivity analysis to the parameter space $x_f \times \beta$ as in §4.2. Fig. 12 shows the sensitivity of the growth rate for Mode 1 (top panel) and Mode 2 (bottom panel). Thick black lines correspond to the zero growth rate level sets of Fig. 9, and thin light lines to the zero contour lines of the sensitivity maps, i.e., the lines along which the system is insensitive to small changes in the convection speed. Every horizontal slice of Fig. 12 produces a graph analogous to Fig. 11, which corresponds to the horizontal lines highlighted in red at $\beta = 6$. Note that the sensitivity of Mode 1 is actually discontinuous across the lines where one eigenvalue takes over from another, the dashed lines of Fig. 9. This is because, as discussed in §4.2, we are switching eigenvalue along these lines.

Note how in Mode 2's sensitivity map, the zero growth-rate isolines cross the zero sensitivity isolines at the acoustic nodes $x_f \approx 1/3$ and $2/3$. This is because the location of the nodes is a purely acoustic property, and it is unaffected by a change in the convection speed, which only alters the flow and flame dynamics. Also, note how all the zero sensitivity isolines cross the zero growth rate isolines always in the same fashion in both mode's maps: the lower parts of the neutral curves always lie in regions with a positive sensitivity (light colours), and the upper parts in regions with a negative sensitivity (dark colours). As a consequence, increasing the convection parameter K, shifts the edges of the instability towards a smaller β value, i.e., towards shorter flames. This has a very simple physical explanation: according to the Rayleigh criterion, a thermoacoustic oscillation can occur only when unsteady heat release and acoustic pressure fluctuations are sufficiently in phase. Changing the parameter K does not affect the acoustics, but it does change the phase of heat release fluctuations. In particular, we can relate the time delay of heat release fluctuations with the time that a perturbation needs to travel from the base to the tip, given by:

$$\tau \propto L_f \frac{1}{\overline{U}_c} = \beta R \frac{K}{\overline{U}} \tag{30}$$

The onset of thermoacoustic instabilities is found at specific values of time delays τ. Thus, if we increase the convection parameter K and we wish to find where the new zero

22
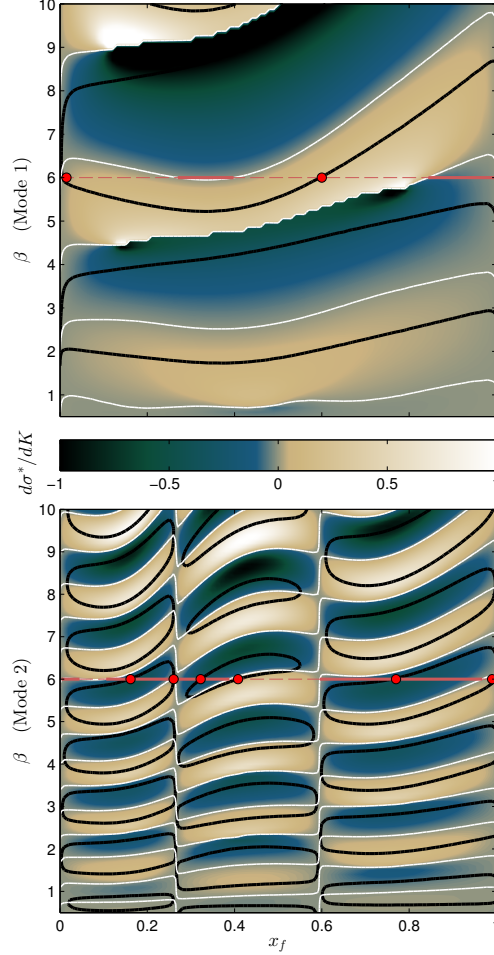
Figure 12: Growth rate sensitivity to convection speed variations in the parameter space $x_f \times \beta$. Thick black lines are the neutral lines of the growth rate map. Thin light lines are the zero contours of the sensitivity maps, i.e., where the system is insensitive to small changes in the parameter K. The red lines highlight results shown in Fig. 11: solid and dashed red lines have a negative and positive sensitivity, respectively.

growth rate contours lies by keeping the time delay constant, then we need to reduce β, in agreement with the sensitivity analysis. This also means that the sensitivities with respect to K and β must have the same sign, because increasing K or β causes an increase in the time delay. This can be verified by qualitatively evaluating $d\sigma^*/d\beta$ along vertical lines in the growth rate maps of Fig. 9.

All the results obtained with adjoint sensitivity are in line with an intuitive physical argument based on the time delay induced by the convection speed model, and can be used to understand changes in the stability of thermoacoustic system's with premixed flames. This example shows how sensitivity analysis has great potential for the design and passive control of thermoacoustic systems, one of its main advantages being that the

process can be embedded within a gradient-based optimization algorithm.

6. Conclusions

In this study we have evaluated Flame Transfer Functions (FTF) for laminar, conical flames excited by an incompressible, travelling wave flow model. We obtain analytical results for the case of uniform flame speeds (which contains a correction to a previously published result), and numerical results when we account for curvature's corrections on the flame speed. We show how in the latter case the numerical evaluation can become unnecessarily expensive even for low-order models. Therefore we tackle the thermoacoustic problem from a different perspective, by avoiding the explicit evaluation of FTFs and directly evaluating the stability of the fully-coupled thermoacoustic system. In this way the stability problem is cast in a classic eigenvalue problem and one can efficiently solve only for the eigenvalues of interest, typically the ones with the largest growth rates. With minimal computational resources we can calculate the stability of the system over a wide range of parameters, and we identify and discuss the location of stability lines (Hopf bifurcations) in the parameter space. Finally, we show how adjoint sensitivity methods can be applied to this model without any further expensive calculation. Sensitivity results help to extract even more information out of the eigenvalue problem. We explicitly evaluate the sensitivity with respect to the convection speed parameter, but any other parameter of the system could be chosen. We observe that the system's stability is strongly connected to the time delay $L_f/\overline{U}_c$ induced by the convective model, as expected. Future analysis can extend them to systems with premixed flames using more elaborated models for the flame and heat release dynamics and to the more sophisticated question of optimizing a burner shape.

Appendix A.

The complete set of non-dimensional variables and parameters we define is:

$$
\begin{aligned}
& x = \frac{\tilde{x}}{L_f} && \beta = \frac{L_f}{R} && r = \frac{\tilde{r}}{R} = \beta \frac{\tilde{r}}{L_f} \\
& \overline{F} = \frac{\tilde{\overline{F}}}{L_f} && f = \frac{\tilde{f}}{L_f} && \nabla = L_f \tilde{\nabla} = \left(\frac{\partial}{\partial x}, \beta \frac{\partial}{\partial r} \right) \\
& t = \tilde{t} \frac{\overline{U}}{L_f} && St = \frac{\omega L_f}{\overline{U}} && K = \frac{\overline{U}}{\overline{U}_c} = \frac{k L_f}{St} \\
& u_x = \frac{\tilde{u}_x}{\overline{U}} && u_r = \frac{\tilde{u}_r}{\overline{U}} && \frac{\tilde{s}_L^0}{\overline{U}} = \frac{1}{\sqrt{1 + \beta^2}} \\
& \kappa = \tilde{\kappa} L_f && \mathcal{M} = \frac{\mathcal{L}}{L_f} && \sin \alpha(r) = \left[1 + \beta^2 \left(\frac{d\overline{F}}{dr} \right)^2 \right]^{-1/2}
\end{aligned}
\tag{A.1}
$$

Appendix B.

The eigenvalue problem we want to solve reads:

$$
-\frac{\beta^2}{\sqrt{1 + \beta^2}} \left(h_1(r) \frac{d\hat{f}}{dr} + h_2(r) \frac{d^2\hat{f}}{dr^2} \right) + \left(\hat{u}_x' + \frac{r}{2} \frac{d\overline{F}}{dr} \frac{d\hat{u}_x'}{dx} \right)_{x=\overline{F}} = \lambda \hat{f}
\tag{B.1a}
$$

$$
\mathcal{A}\hat{s} + \mathcal{B} \frac{\beta^2}{2\sqrt{1 + \beta^2}} \int_0^1 \left(h_1(r) \frac{d\hat{f}}{dr} + h_2(r) \frac{d^2\hat{f}}{dr^2} r \right) dr = \lambda \hat{s}
\tag{B.1b}
$$

$$
-\frac{1}{K} \frac{d\hat{u}_x'}{dx} = \lambda \hat{u}_x'
\tag{B.1c}
$$

where h_1 and h_2 are functions of the mean flame shape only, obtained by inspection from the relation:

$$
h_1(r) \frac{d\hat{f}}{dr} + h_2(r) \frac{d^2\hat{f}}{dr^2} = \left(\sin \alpha \frac{d\overline{F}}{dr} + 2\mathcal{M}\beta^2 \sin^4 \alpha \frac{d\overline{F}}{dr} \frac{d^2\overline{F}}{dr^2} - \mathcal{M} \frac{1}{r} \right) \frac{d\hat{f}}{dr} - \mathcal{M} \sin^2 \alpha \frac{d^2\hat{f}}{dr^2}
$$

We discretize the radial and axial components into:

$$
r \rightarrow \boldsymbol{r} = [r_0 = 1, r_1, \ldots, r_j, \ldots, r_{N_r+1} = 0]
$$

$$
\hat{f}(r) \rightarrow \hat{f}(\boldsymbol{r}) = \hat{\boldsymbol{f}} = \left[\hat{f}^0, \hat{f}^1, \ldots, \hat{f}^j, \ldots, \hat{f}^{N_r+1} \right]
\tag{B.2}
$$

and

$$
x \rightarrow \boldsymbol{x} = [x_0 = 0, x_1, \ldots, x_j, \ldots, x_{N_x+1}]
$$

$$
\hat{u}_x'(x) \rightarrow \hat{u}_x'(\boldsymbol{x}) = \hat{\boldsymbol{u}}_x' = \left[\hat{u}_x'^0, \hat{u}_x'^1, \ldots, \hat{u}_x'^j, \ldots, \hat{u}_x'^{N_x+1} \right]
\tag{B.3}
$$

where $N_r + 2$ is the number of discretization point for the flame, and $N_x + 2$ the number of discretization points for the velocity field, which has to be sufficiently high to store

the value of the axial velocity inside the flame. Also, the velocity has to be evaluated at the mean flame positions: it is therefore natural to discretize the radial and axial directions with the same number of points, i.e., $N_r = N_x$ with $\boldsymbol{x} = \overline{F}(\boldsymbol{r})$. The boundary conditions (7) determine the flame position at $r = 0$ and $r = 1$, so we are left with N_r degrees of freedom. We indicate with D_x, D_r and $D_{r,r}$ the $(N_r + 2) \times (N_r + 2)$ first and second differentiation matrices in the axial and radial directions respectively; D_x and D_r differ because if $\mathcal{M} \neq 0$, the steady solution is not a straight line, and the discretization in the axial direction is non-uniform. Finally, the heat release integration is discretized as:

$$
\int_0^1 \left(h_1(r)\frac{d\hat{f}}{dr} + h_2(r)\frac{d^2\hat{f}}{dr^2} \right) r\, dr \approx \sum_{k=0}^{N_r+1} \Delta r\, \mu_k\, r_k \left(h_1(r_k)\left.\frac{d\hat{f}}{dr}\right|_k + h_2(r_k)\left.\frac{d^2\hat{f}}{dr^2}\right|_k \right) =
$$

$$
= \sum_{k=0}^{N_r+1} \sum_{j=1}^{N_r} \Delta r\, \mu_k\, r_k \left(h_1^k D_r^{k,j} \hat{f}^j + h_2^k D_{r,r}^{k,j} \hat{f}^j \right) = \tag{B.4}
$$

$$
= \sum_{j=1}^{N_r} \left[\sum_{k=0}^{N_r+1} \Delta r\, \mu_k\, r_k \left(h_1^k D_r^{k,j} + h_2^k D_{r,r}^{k,j} \right) \right] \hat{f}^j = \sum_{j=1}^{N_r} \Delta q^j\, \hat{f}^j
$$

460 where μ_k are weights of the integral discretization chosen.

We can finally express the submatrices of the eigenvalue problem as (23), defining:

$$
M_{ff}^{i,j} = -\frac{\beta^2}{\sqrt{1+\beta^2}} \left(h_1^i D_r^{i,j} + h_2^i D_{r,r}^{i,j} \right) \qquad i = 1,\dots,N_r \qquad j = 1,\dots,N_r \tag{B.5a}
$$

$$
M_{fs}^{i,j} = \frac{1}{2}r_i \left.\frac{d\overline{F}}{dr}\right|_i \xi_i \left(\delta_{1,i} + \delta_{2,i} \right) \mathcal{C}_u^j \qquad i = 1,\dots,N_r \qquad j = 1,\dots,N_s \tag{B.5b}
$$

$$
M_{fu}^{i,j} = \delta_{i,j} + \frac{1}{2}r_i \left.\frac{d\overline{F}}{dr}\right|_i D_x^{i,j} \qquad i = 1,\dots,N_r \qquad j = 1,\dots,N_x \tag{B.5c}
$$

$$
M_{sf}^{i,j} = \frac{\beta^2}{2\sqrt{1+\beta^2}} \mathcal{B}^i \Delta q^j \qquad i = 1,\dots,N_s \qquad j = 1,\dots,N_r \tag{B.5d}
$$

$$
M_{ss}^{i,j} = \mathcal{A}^{i,j} \qquad i = 1,\dots,N_s \qquad j = 1,\dots,N_s \tag{B.5e}
$$

$$
M_{su}^{i,j} = 0 \qquad i = 1,\dots,N_s \qquad j = 1,\dots,N_x \tag{B.5f}
$$

$$
M_{uf}^{i,j} = 0 \qquad i = 1,\dots,N_x \qquad j = 1,\dots,N_r \tag{B.5g}
$$

$$
M_{us}^{i,j} = -\frac{1}{K}\xi_i \left(\delta_{1,i} + \delta_{2,i} \right) \mathcal{C}_u^j \qquad i = 1,\dots,N_x \qquad j = 1,\dots,N_s \tag{B.5h}
$$

$$
M_{uu}^{i,j} = -\frac{1}{K}D_x^{i,j} \qquad i = 1,\dots,N_x \qquad j = 1,\dots,N_x \tag{B.5i}
$$

461 where $\delta_{i,j}$ is the Kronecker delta, and ξ_i are finite difference coefficients which apply
462 the boundary condition (22) for the velocity at the flame base; because we use a second
463 order scheme, only two of them are non-zero.

464 **References**

465 [1] F. E. C. Culick, Unsteady Motions in Combustion Chambers for Propulsion Systems, AGARDo-
466   graph, RTO AG-AVT-039, 2006.

26

467   [2] T. C. Lieuwen, Unsteady combustor physics, Cambridge University Press, 2012.
468   [3] A. L. Birbaud, D. Durox, S. Candel, Combustion and Flame 146 (2006) 541–552.
469   [4] Preetham, S. Hemchandra, T. Lieuwen, Journal of Propulsion and Power 24 (2008) 1390–1402.
470   [5] T. Schuller, S. Ducruix, D. Durox, S. Candel, Proceedings of the Combustion Institute 29 (2002)
471   107–113.
472   [6] T. Schuller, D. Durox, S. Candel, Combustion and Flame 134 (2003) 21–34.
473   [7] N. Karimi, M. J. Brear, S. H. Jin, J. P. Monty, Combustion and Flame 156 (2009) 2201–2212.
474   [8] A. Cuquel, D. Durox, T. Schuller, in: 7th Mediterranean Combustion Symposium, Chia Laguna,
475   Cagliari, Sardinia, Italy,.
476   [9] A. Cuquel, D. Durox, T. Schuller, Proceeding of the Combustion Institute 34 (2013) 1007–1014.
477   [10] K. Kashinath, S. Hemchandra, M. P. Juniper, Combustion and Flame 160 (2013) 2856–2865.
478   [11] T. Lieuwen, Journal of Propulsion and Power 19 (2003) 765–781.
479   [12] H. Y. Wang, C. K. Law, T. Lieuwen, Combustion and Flame 156 (2009) 889–895.
480   [13] Preetham, S. K. Thumuluru, T. Lieuwen, S. Hemchandra, Journal of Propulsion and Power 26
481   (2010) 524–532.
482   [14] N. Noiray, D. Durox, T. Schuller, S. Candel, Journal of Fluid Mechanics 615 (2008) 139–167.
483   [15] L. Kabiraj, R. I. Sujith, Journal of Fluid Mechanics 713 (2012) 376–397.
484   [16] F. Creta, M. Matalon, Proceedings of the Combustion Institute 33 (2011) 1087–1094.
485   [17] A. Cuquel, D. Durox, T. Schuller, Comptes Rendus - Mecanique 341 (2013) 171–180.
486   [18] G. J. Bloxsidge, A. P. Dowling, P. J. Langhorne, Journal of Fluid Mechanics 193 (1988) 445–473.
487   [19] D. Sipp, O. Marquet, P. Meliga, A. Barbagallo, Applied Mechanics Reviews 63 (2010) 030801.
488   [20] P. Luchini, A. Bottaro, Annual Review of Fluid Mechanics 46 (2014) 493–517.
489   [21] L. Magri, M. P. Juniper, Journal of Fluid Mechanics 719 (2013) 183–202.
490   [22] L. Magri, M. P. Juniper, Journal of Fluid Mechanics 752 (2014) 237–265.
491   [23] G. Darrieus, in: 6th International Congress of Applied Mechanics, Paris. Unpublished work.
492   [24] L. Landau, Acta physicochimica 19 (1944) 77–85.
493   [25] V. Moureau, B. Fiorina, H. Pitsch, Combustion and Flame 156 (2009) 801–812.
494   [26] L. Humphrey, V. Acharya, D. H. Shin, T. Lieuwen, International Journal of Spray and Combustion
495   Dynamics 6 (2014) 411–416.
496   [27] G. H. Markstein, Non-steady Flame Propagation Pergamon, 1964.
497   [28] S. Gottlieb, C. W. Shu, Mathematics of Computation of the American Mathematical Society 67
498   (1998) 73–85.
499   [29] D. H. Shin, T. Lieuwen, Journal of Fluid Mechanics 721 (2013) 484–513.
500   [30] S. Hemchandra, Combustion and Flame 159 (2012) 3530–3543.
501   [31] M. Blanchard, T. Schuller, D. Sipp, P. J. Schmid, Physics of Fluids 27 (2015) 043602.
502   [32] A. P. Dowling, Journal of Fluid Mechanics 394 (1999) 51–72.
503   [33] K. Kashinath, S. Hemchandra, M. P. Juniper, Journal of Engineering for Gas Turbines and Power
504   135 (2013) 061502.
505   [34] I. C. Waugh, K. Kashinath, M. P. Juniper, Journal of Fluid Mechanics 759 (2014) 1–27.
506   [35] A. Orchini, S. J. Illingworth, M. P. Juniper, Journal of Fluid Mechanics 775 (2015) 387–414.
507   [36] H. Mangesius, W. Polifke, International Journal of Spray and Combustion Dynamics 3 (2011) 331–
508   350.
509   [37] M. R. Bothien, J. P. Moeck, A. Lacarelle, C. O. Paschereit, Journal of Power and Energy 221 (2007)
510   657–668.
511   [38] F. Giannetti, P. Luchini, Journal of Fluid Mechanics 581 (2007) 167–197.
512   [39] G. J. Chandler, M. P. Juniper, J. W. Nichols, P. J. Schmid, Journal of Computational Physics 231
513   (2012) 1900–1916.
514   [40] A. Orchini, M. P. Juniper, Proceedings of ASME Turbo Expo (2015) GT2015–43219.
515   [41] R. Hartmann, SIAM Journal on Numerical Analysis 45 (2007) 2671–2696.

27